Proceedings of the 9th World Congress on Mechanical, Chemical, and Material Engineering (MCM'23)
Brunel University, London, United Kingdom –August 06-08, 2023
Paper No. HTFF 152
DOI: 10.11159/htff23.152

Droplet Statistics and Vorticity Evolution of Immiscible Rayleigh-Taylor Turbulence

Dongxiao Zhao[1], Gaojin Li[2]
[1]School of Engineering Mechanics,
Shanghai Jiao Tong University, Shanghai 200240, PR China

Abstract **-** Ubiquitous in many natural and engineering flows, Rayleigh-Taylor (RT) instability and the ensuing turbulence develop when heavy fluid is placed on top of light fluid under gravity. Compared to the miscible cases, RT instability between two immiscible fluids encompasses more complex physics due to the presence of the sharp interface. To elucidate its physical mechanism, we perform direct numerical simulations using the volume of fluid approach and analyse their dynamical evolution, including statistics such as the kinetic energy and vorticity budgets, droplet size distribution, and the turbulent anisotropy. We show that the surface tension contribution is negligible for mean kinetic energy, but it plays a major role in the mean vorticity budget. During the immiscible RT evolution, the distribution of droplet sizes follows the -10/3 scaling in compatible with the Kolmogorov-Hinze theory for isotropic two-phase turbulence, although the flow is inhomogeneous and anisotropic. Numerical results further show that the droplets are effective in modulating both large-scale and small-scale flow quantities.

Keywords**:** Rayleigh-Taylor turbulence, two-phase flow, droplet size distribution, kinetic energy budget, vorticity budget

1. Introduction

High Reynolds number flows involving two or more immiscible phases find important applications in many natural and engineering systems such as atmospheric and oceanic flows [1], combustion [2], food processing [3], and pharmaceuticals [4]. Central topics of multiphase turbulence are the transport and mixing of different species, which depend on the droplet/bubble size distribution arising from the turbulence coupling with the breakup and coalescence processes. Better understandings of the droplet/bubble statistics could in principle improve the design of industrial applications for food emulsification [5], oil recovery [6], and clean power generation [7].

Turbulent two-phase flows in homogeneous and isotropic configurations have been studied extensively via direct numerical simulations (DNS) [8-11]. For example, Dodd and Ferrante [8] performed DNS of decaying isotropic two-phase turbulence with varying Weber numbers, densities and viscosity ratios using the volume-of-fluid (VOF) approach. They quantitatively characterized the kinetic energy exchange pathways between the carrier phase and the droplet phase, and found that droplets enhance the dissipation rate of turbulent kinetic energy by enhancing the local velocity gradients near the interface. The power of surface tension could act as a sink or a source for kinetic energy depending on the sign of the rate-of-change of the total droplet surface area. Mukherjee et al. [9] performed DNS of homogeneous isotropic emulsions using lattice Boltzmann method, and proposed a generalized Hinze scale based on a Weber number spectrum. They further identified a time-delayed quasi-equilibrium cycle in the state-space of the system comprising kinetic energy, enstrophy, and the droplet number density. Perlekar's phase-field pseudo-spectral simulations [10] indicate that the interfacial terms provide another route for turbulent energy cascade, and the statistics associated with velocity-gradient tensor does not change with the Weber number. Crialesi-Esposito et al. [11] simulated the iso-density emulsions with different volume fractions, viscosity ratios, and Weber numbers using the VOF approach, and confirmed the forward energy cascade by performing a scale-by-scale analysis. These findings greatly improve our fundamental understanding of multiphase turbulence, and provide insights for studying more complicated, real-world multiphase flows.

Besides homogeneous, isotropic cases, studies on immiscible two-fluid turbulence in more complicated configurations start to emerge recently. Yi et al. [12] experimentally investigated the droplet size distribution and the physical mechanism of droplet breakup in turbulent Taylor-Couette flows. They introduced an effective viscosity in high volume-fraction systems and related it to the droplet statistics. Rosti et al. [13] numerically verified that the Hinze maximum stable droplet size estimation is valid in a two-phase turbulent shear flow, even though the Hinze theory assumes isotropic turbulence and no coalescence. Trummler et al. [14] studied the segregation of turbulent emulsions

under gravity and identified different roles played by gravity and droplet coalescence. The timescale of the segregation is proposed using dimensional arguments.

Although the above investigations in non-isotropic configurations have addressed a few issues, many important questions are still open. For example, real-world problems are usually time-dependent, and it is important to characterize how the droplet size distribution varies in time. In addition, understanding the evolution of vorticity and strain in a time-dependent multiphase turbulence would help gain insights into the small-scale flow physics. To address these questions, we perform direct numerical simulations and consider a classical problem, the Rayleigh-Taylor (RT) turbulence between two immiscible fluids with comparable densities. The RT instability occurs when a heavy fluid is placed on top of a light one and develops coherent bubble and spike structures, leading to a devolving multiphase turbulence. We then analyse the statistics of RT turbulent flows, focusing on the vorticity evolution, droplet size distribution, and its associated dynamics.

The following sections are organized as follows. In section 2 we present the governing equations and numerical methods for our direct numerical simulation. In section 3 we show the results and analysis, including flow visualizations, the energy and enstrophy budgets, and the droplet statistics. In section 4 we summarize and conclude our paper.

2. Numerical Methods

We adopt the Volume of Fluid approach to perform the direct numerical simulation of immiscible two-phase Rayleigh-Taylor turbulence, the governing equations include the equations of continuity, momentum, and the marker function advection, which read

$$\nabla \cdot \mathbf{u} = 0 \tag{1}$$

$$\rho\left(\frac{\partial}{\partial t} + \mathbf{u}\cdot\nabla\right)\mathbf{u} = -\nabla P + \rho\mathbf{g} + \nabla\cdot\boldsymbol{\tau} + \sigma\kappa\nabla c \tag{2}$$

$$\left(\frac{\partial}{\partial t} + \mathbf{u}\cdot\nabla\right)c = 0 \tag{3}$$

where $\rho, \boldsymbol{u}, c$ are the density, velocity, and marker function, respectively. $\boldsymbol{g}, \sigma, \kappa$ are the gravitational acceleration, surface tension coefficient, and the interface curvature, $\boldsymbol{\tau} = \mu(\nabla\boldsymbol{u} + \nabla\boldsymbol{u}^T)$ is the viscous stress tensor, with μ the dynamic viscosity.

The simulations are conducted with the open-source package PARIS (PArallel, Robust, Interface Simulator) [15], which is design for simulating multiphase flows and has been widely adopted to study atomization [16], multiphase mixing layer [17,18], and segregation [14]. The code advances in time using a second-order predictor-corrector scheme, while for spatial discretization the viscous term is calculated explicitly with a second-order central difference and the Superbee limiter is applied in the flux calculation. A finite-volume staggered grid is adopted where the velocity fields are stored on cell faces and marker function as well as pressure are stored at cell centres. The pressure Poisson equation is solved with the PFMG multigrid solver. More details on the numerical schemes can be found in reference [15].

For the Rayleigh-Taylor simulations, the domain is set to be $L_x \times L_y \times L_z = 1.6 \times 1.6 \times 3.2$, which is discretised into uniform cells with cell number $256 \times 256 \times 512$. The initial conditions are set with heavy fluid on top of light fluid, with the initial interface horizontal and a small perturbation imposed. In this paper, we choose the densities of heavy and light fluids to be $\rho_h = 1.0, \rho_l = 0.9$, and thus the non-dimensional Atwood number is $At = (\rho_h - \rho_l)/(\rho_h + \rho_l) = 0.0526$. We simulate two cases with the heavy fluid volume fraction to be $\langle c\rangle = 0.95$ and $\langle c\rangle = 0.05$ respectively, denoted by run_95 and run_05 respectively, where c is the marker function for the heavy fluid and $\langle\cdot\rangle$ denotes the spatial mean value. The kinematic viscosity and the surface tension coefficient are $\nu = 2.55 \times 10^{-4}, \sigma = 5 \times 10^{-5}$. The boundary conditions are set to be no-slip walls at the top and the bottom, and periodic conditions are imposed on lateral boundaries.We run the two Rayleigh-Taylor cases run_95 and run_05 from the onset till the decaying stage of the instability. The following sections show the visualizations and statistics of the simulation results.

3. Results

In this section, we present simulation results and the turbulent statistics, focusing on the droplet size distribution and the role of vorticity in the evolution of the Rayleigh-Taylor instability.

3.1. Flow visualization and bulk statistics

We show the flow visualizations in figure 1, in which panels (a)-(c) are from the case run_95 where the volume fraction of the top heavy fluid is 0.95, and panels (d)-(f) are from the case run_05 where the volume fraction of the top heavy fluid is 0.05. We observe droplets creation during the evolution of the RT instability in both cases, and the droplet density varies in time and in space, which we shall quantify in later sections.

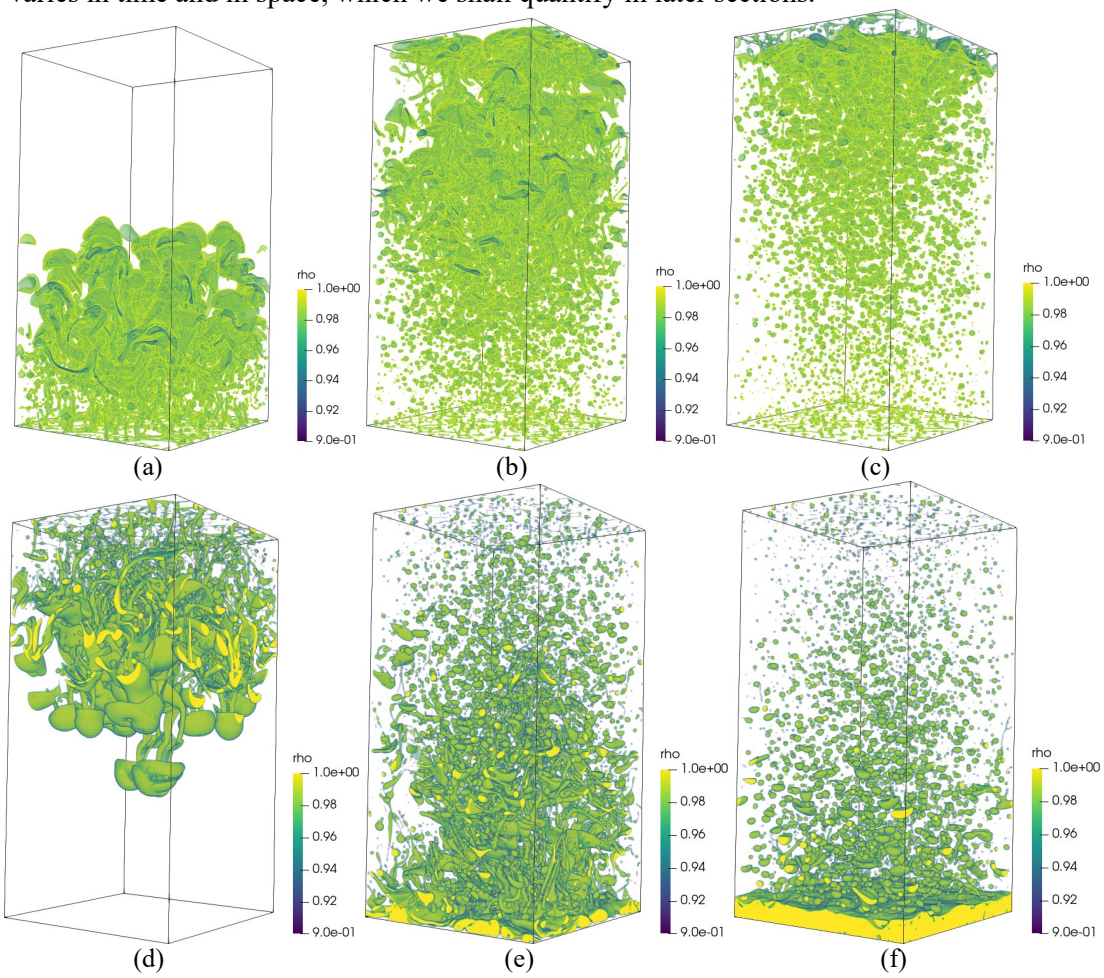

Fig. 1: Visualizations of the density field for the two simulation case, (a)-(c) are from run_95, and (d)-(f) are from run_05. (a),(d) are selected at dimensionless time $\hat{t} = t\sqrt{\frac{Atg}{L}} = 4.53$, (b),(e) at $\hat{t} = 8.16$, and (c),(f) at $\hat{t} = 11.79$

For a quantitative description of the flow, we first show the budget of kinetic energy and vorticity. The bulk kinetic energy (KE) balance equation is:

$$\frac{d}{dt}\left\langle \frac{1}{2}\rho|\boldsymbol{u}|^2 \right\rangle = -\langle \boldsymbol{\tau}:\boldsymbol{S} \rangle + \langle \boldsymbol{u}\cdot\boldsymbol{f}_\sigma \rangle + \langle \rho \boldsymbol{g}\cdot\boldsymbol{u} \rangle$$

where $\boldsymbol{f}_\sigma = \sigma\kappa\nabla c$ is the surface tension, and $\langle\cdot\rangle$ denotes spatial averaging. Terms on the right-hand side denotes viscous dissipation, power of surface tension, and potential energy injection, respectively. The budgets of the two simulation cases are shown in figure 2, in which the time is normalized as $\hat{t} = t\sqrt{At\ g/L}$.

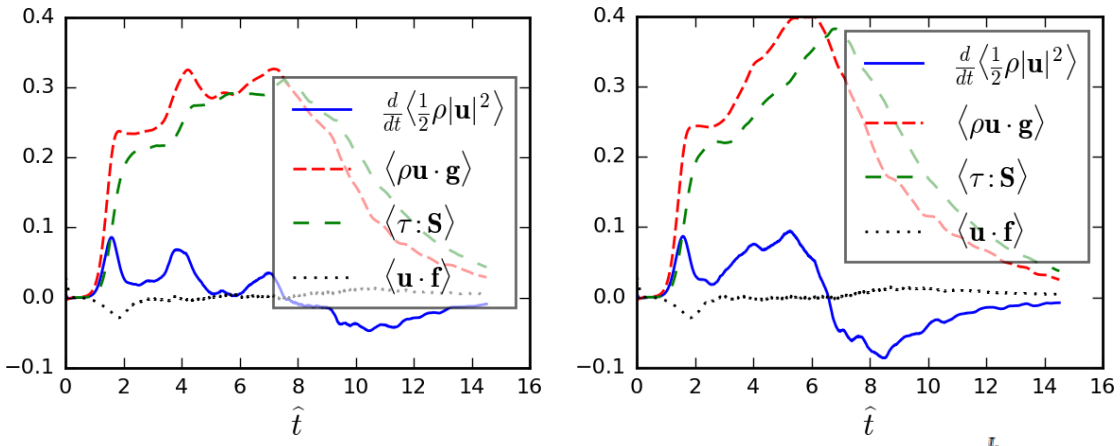

Fig. 2: The evolution of kinetic energy budget, normalized by the mean kinetic energy growth rate $At\,g\frac{L}{T}$. Left figure is for case run_95, and the right figure is for run_05.

From figure 2, the major part of the injected potential energy is balanced by viscous dissipation, and the time derivative of total KE is positive at early time and negative at later time, indicating that KE increases during the developing stage and decreases at the decaying stage of RT. In contrast, the mean power of surface tension is negative at the developing stage and acts as a sink for KE, while it is positive at the decaying stage and acts as a source for KE, in accordance with reference [8]. The magnitude of mean surface tension is small compared to other terms, but its local contribution could be large as indicated by its probability density function (not shown here).

The vorticity budget is represented by the enstrophy evolution equation

$$\frac{d}{dt}\left\langle\frac{1}{2}\rho|\boldsymbol{\omega}|^2\right\rangle = \langle\rho\boldsymbol{\omega}\cdot\nabla\boldsymbol{u}\cdot\boldsymbol{\omega}\rangle + \left\langle\frac{1}{\rho}\boldsymbol{\omega}\cdot(\nabla\rho\times\nabla P)\right\rangle + \left\langle\rho\boldsymbol{\omega}\cdot\nabla\times\left(\frac{1}{\rho}\nabla\cdot\boldsymbol{\tau}\right)\right\rangle + \left\langle\rho\nabla\times\frac{\boldsymbol{f}_\sigma}{\rho}\right\rangle$$

where on the right-hand side, the first term denotes the vortex stretching contribution, the second term denotes the baroclinic vorticity generation, the third term is viscous contribution, while the last term is vorticity generation by surface tension.

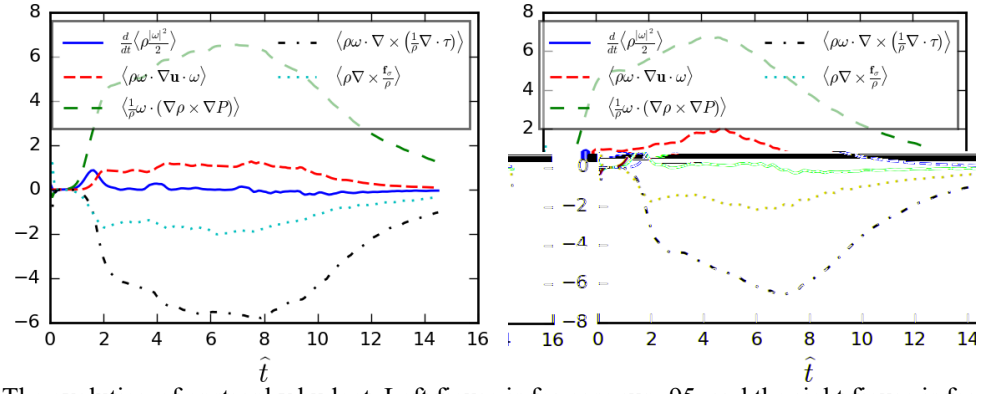

Fig. 3: The evolution of enstrophy budget. Left figure is for case run_95, and the right figure is for run_05.

Figure 3 shows the evolution of enstrophy budget. The time derivative of enstrophy, similar to KE, is positive at early stage as the instability develops, and attains negative values at late stage when the instability decays. Both the baroclinic term and the viscous term are large in magnitude but with opposite signs, and they are singly-peaked with a small-time lag between the two peaks. Similarly, the vortex stretching term and the surface tension term are opposite in sign with relatively smaller magnitude. The cancelling effect between these four terms leads to the alternating positive-negative

values in the time derivative of enstrophy. In contrast to the mean KE budget where surface tension contribution is negligible, it plays a major role in the enstrophy budget, indicating that surface tension is more important at small compared to large scales.

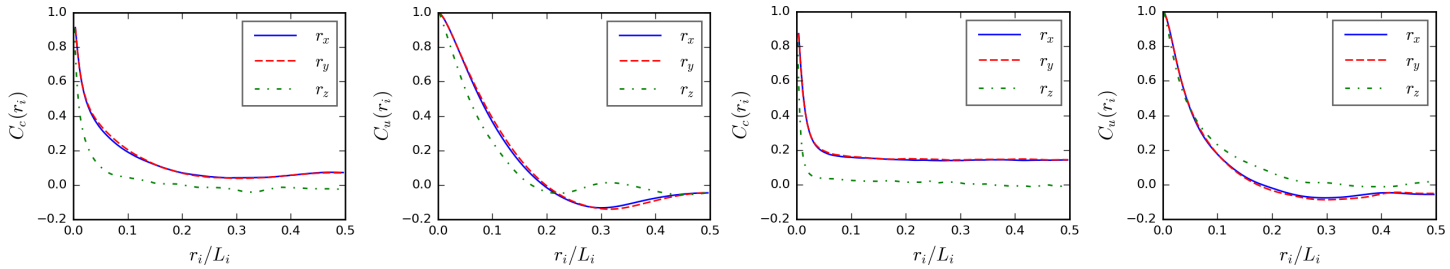

(a) (b)

Fig. 4: Autocorrelation coefficients of the volume fraction and velocity. Panel (a) is for case run_95, while panel (b) is for run_05.

To characterize the anisotropy of the immiscible RT instability, we measure the autocorrelation coefficients of the volume fraction field $C_c(\boldsymbol{r})$ and the velocity field $C_u(r)$, which are defined as

$$C_c(\boldsymbol{r}) = \frac{\langle c(\boldsymbol{x}+\boldsymbol{r})c(\boldsymbol{x})\rangle}{\langle c(\boldsymbol{x})^2\rangle}, \qquad C_u(\boldsymbol{r}) = \frac{\langle \boldsymbol{u}(\boldsymbol{x}+\boldsymbol{r})\cdot\boldsymbol{u}(\boldsymbol{x})\rangle}{\langle \boldsymbol{u}(\boldsymbol{x})\cdot\boldsymbol{u}(\boldsymbol{x})\rangle}$$

Figure 4 shows the results of the autocorrelation, with the subscript i in the figure denoting either x, y or z direction. The results correspond to separation vector $\boldsymbol{r}$ along the x and y directions almost overlap, but are different from the results along the z direction. This behaviour indicates isotropy in the horizontal plane, but anisotropy exists between the horizontal and the vertical directions. Note that the correlation coefficient does not go to zero at large separation distances for the volume fraction field, indicating that the volume fraction field is not fully turbulent for the current configuration.

3.2. Droplet distribution and dynamics

To gain insights into the physics of immiscible RT turbulence, we measure the droplet distribution and delineate the underlying physics in this subsection. The time evolution of the number of droplets is shown in figure 5, in which both simulation cases follow a similar pattern. The total number increases till maximum values attained around $\hat{t} \approx 9$, and then decreases in the decaying stage of RT instability. More refined information can be inferred from figure 1, where droplets of different sizes can be observed at different time instants.

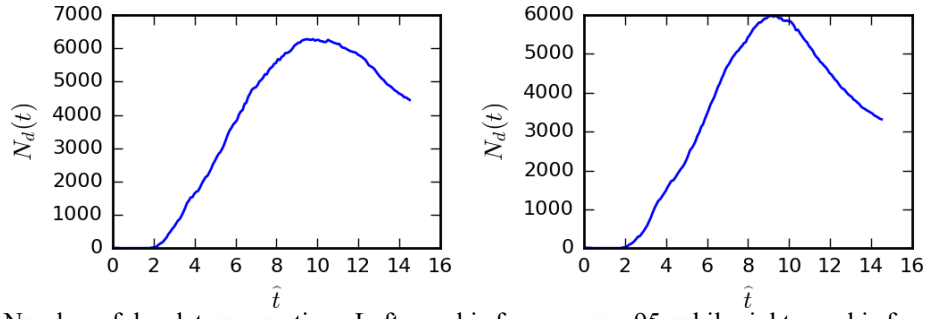

Fig. 5: Number of droplets versus time. Left panel is for case run_95, while right panel is for run_05.

To quantify the sizes of droplets, we obtain in figure 6 the probability density functions (PDFs) of droplet diameter $P(d)$ at each of the three instants $\hat{t} = 4.53, 8.16, 11.79$, corresponding to the developing stage, the maximum droplet number instant, and the decaying stage of RT. A $d^{-10/3}$ scaling in compatible with the Kolmogorov-Hinze theory is included. The PDFs show that the difference between the three instants is mainly at the tail of the PDFs corresponding to large droplets. A general trend is that the number of large droplets decreases in time, while the size

distribution of small droplets remains unchanged. At $\hat{t} = 4.53$ and 8.16 the $d^{-10/3}$ scaling is realized within a small diameter range, indicating that, although the isotropic assumption is invalid, the result of Kolmogorov-Hinze theory for for droplet size distribution is applicable to the inhomogeneous anisotropic Rayleigh-Taylor turbulent flows.

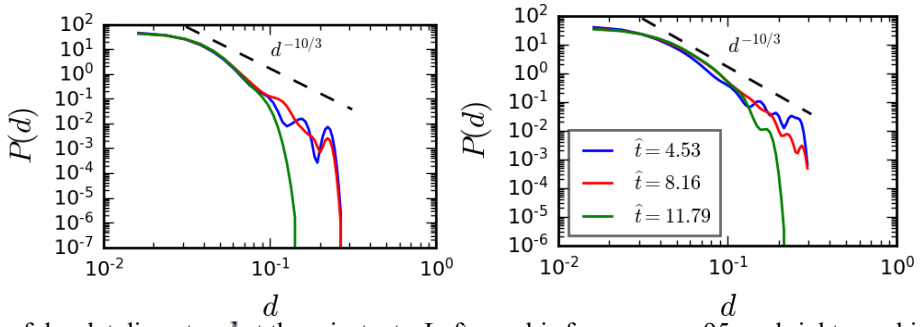

Fig. 6: PDFs of droplet diameter d at three instants. Left panel is for case run_95, and right panel is for run_05.

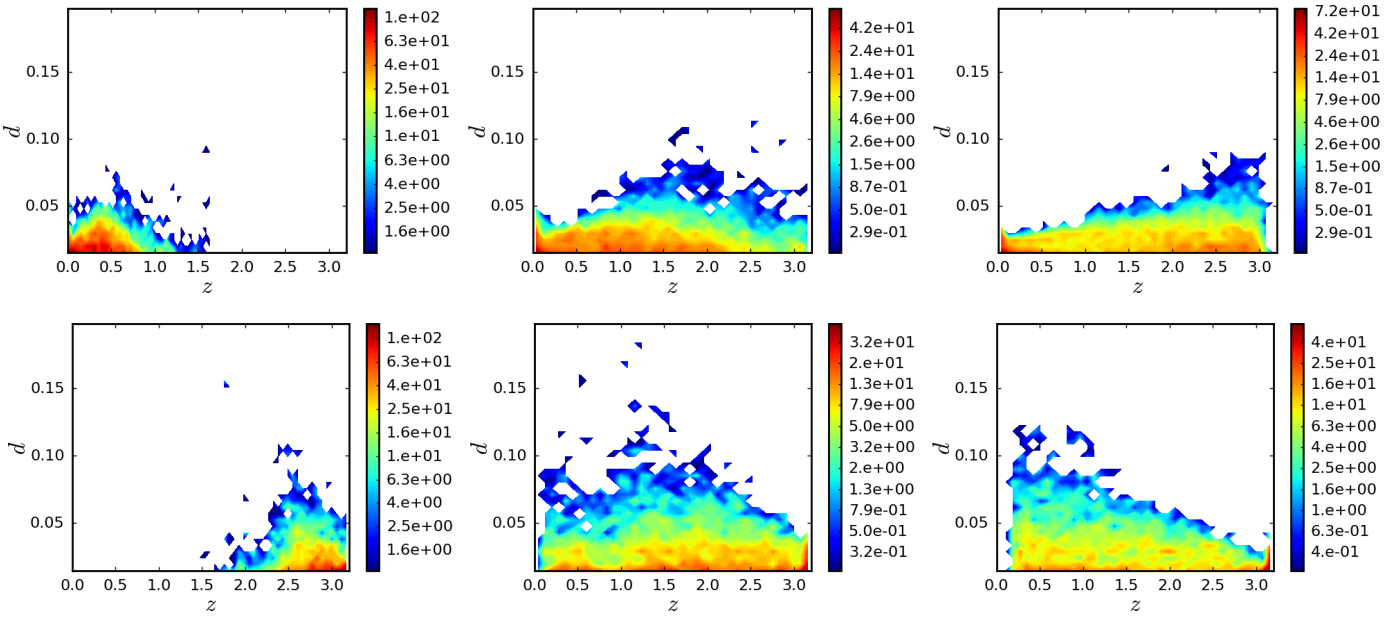

Fig. 7: Joint PDFs of droplet diameter d with its center z location at three instants. Top three panel are for case run_95, while the bottom three panels are for run_05. The three colums correspond to time $\hat{t} = 4.53, 8.16, 11.79$, respectively.

The spatial distribution of droplets is demonstrated in figure 7, in which the joint PDFs between the droplet diameter and the z location of droplet centers are plotted. For the case run_95, the heavy-light fluid interface tends to rise from the bottom to the top, and thus the generated droplets migrate upwards; while for the case run_05, the heavy-light fluid interface sinks from the top to the bottom, and thus the droplets migrate downwards. It is also confirmed (not shown here) that the z-location of the large diameter droplets (the z-location of the peak in each of the joint PDFs in figure 7) resides upstream of the maximum turbulent intensity, indicating that turbulent fluctuations tend to distort the large droplets and lead to break up into smaller droplets.

As for the dynamics of the droplets, we shown in figures 8 and 9 the joint PDFs of diameter with the mean vertical velocity and the mean enstrophy corresponding to each droplet. Large droplets are associated with large mean V_z (in magnitude) and large mean enstrophy, highlighting the role of large droplets in modulating both large-scale velocity and small-scale vorticity.

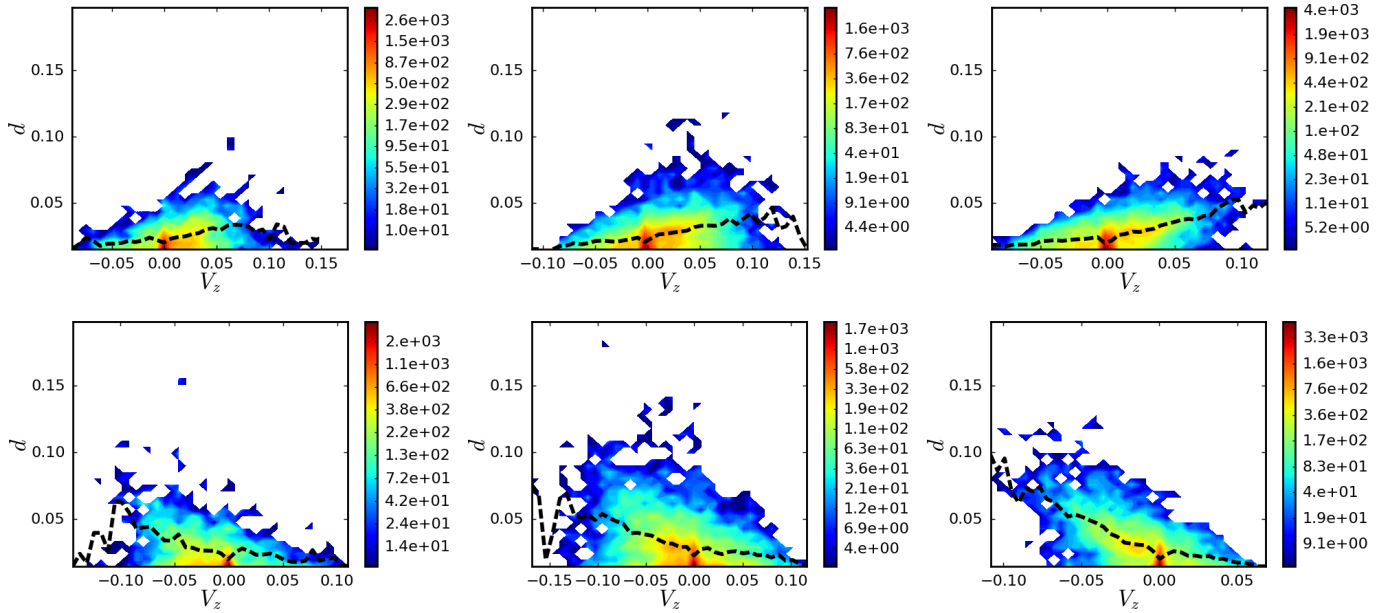

Fig. 8: Joint PDFs of droplet diameter d with the droplet mean vertical velocity. Top three panel are for case run_95, while the bottom three panels are for run_05. The three colums correspond to time $\hat{t} = 4.53, 8.16, 11.79$, respectively.

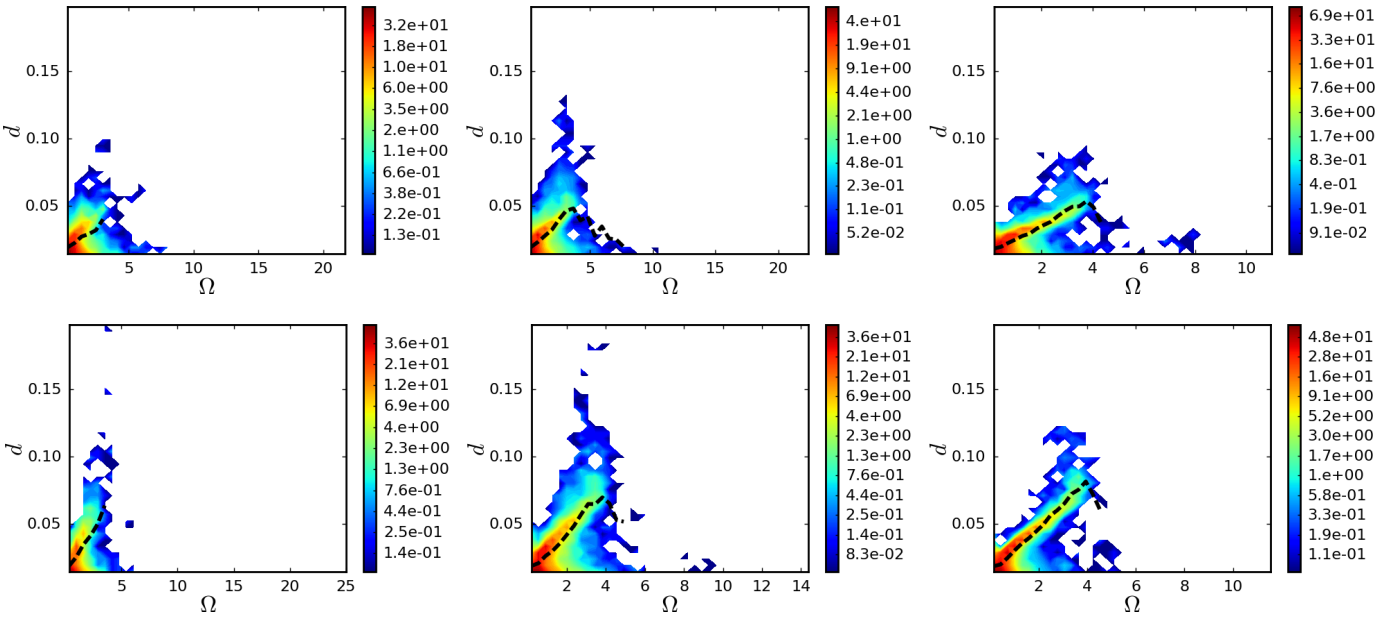

Fig. 9: Joint PDFs of droplet diameter d with the droplet mean enstrophy. Top three panel are for case run_95, while the bottom three panels are for run_05. The three colums correspond to time $\hat{t} = 4.53, 8.16, 11.79$, respectively.

4. Conclusion

In this short paper, we investigate the statistics and dynamics of immiscible two-fluid Rayleigh-Taylor turbulence. We find that the surface tension term plays little role in the large-scale mean kinetic energy budget, but is important in

the small-scale mean enstrophy budget. The immiscible Rayleigh-Taylor turbulence is anisotropic along the horizontal and vertical directions as measured by the autocorrelation of volume fraction and velocity fields. From the droplet statistics, we find that the -10/3 Kolmogorov-Hinze scaling is still applicable, and the droplet spatial distribution is inhomogeneous and depends on the turbulent intensity which enchances large droplet breakup. The large droplets are associated with large velocity and vorticity magnitude, emphasizing its role in both large- and small-scale dynamics of RT turbulence.

Acknowledgements

We thank the support from the Centre for High Performance Computing at Shanghai Jiao Tong University.

References

[1] G. B. Deane and M. D. Stokes, “Scale dependence of bubble creation mechanisms in breaking waves,” Nature, vol. 418, no. 6900, pp. 839–844, 2002.
[2] M. Chmielewski, P. Niszczota, and M. Gieras, “Combustion efficiency of fuel-water emulsion in a small gas turbine,” Energy (Oxf.), vol. 211, no. 118961, p. 118961, 2020.
[3] D. J. McClements, “Emulsion design to improve the delivery of functional lipophilic components,” Annu. Rev. Food Sci. Technol., vol. 1, no. 1, pp. 241–269, 2010.
[4] A. Spernath and A. Aserin, “Microemulsions as carriers for drugs and nutraceuticals,” Adv. Colloid Interface Sci., vol. 128–130, pp. 47–64, 2006.
[5] D. J. McClements, Food emulsions: Principles, practices, and techniques, third edition. London, England: CRC Press, 2015.
[6] S. Kokal, “Crude-oil emulsions: A state-of-the-art review,” SPE Prod. Facil., vol. 20, no. 01, pp. 5–13, 2005.
[7] C. Heinrich, H. Dörksen, A. Esch, and K. Krämer, “Gasoline water direct injection (GWDI) as a key feature for future gasoline engines,” in Knocking in Gasoline Engines, Cham: Springer International Publishing, 2018, pp. 322–337.
[8] M. S. Dodd and A. Ferrante, “On the interaction of Taylor length scale size droplets and isotropic turbulence,” J. Fluid Mech., vol. 806, pp. 356–412, 2016.
[9] S. Mukherjee, A. Safdari, O. Shardt, S. Kenjereš, and H. E. A. Van den Akker, “Droplet–turbulence interactions and quasi-equilibrium dynamics in turbulent emulsions,” J. Fluid Mech., vol. 878, pp. 221–276, 2019.
[10] P. Perlekar, “Kinetic energy spectra and flux in turbulent phase-separating symmetric binary-fluid mixtures,” J. Fluid Mech., vol. 873, pp. 459–474, 2019.
[11] M. Crialesi-Esposito, M. E. Rosti, S. Chibbaro, and L. Brandt, “Modulation of homogeneous and isotropic turbulence in emulsions,” J. Fluid Mech., vol. 940, no. A19, 2022.
[12] L. Yi, C. Wang, S. G. Huisman, and C. Sun, “Recent developments of turbulent emulsions in Taylor-Couette flow,” Philos. Trans. A Math. Phys. Eng. Sci., vol. 381, no. 2243, p. 20220129, 2023.
[13] M. E. Rosti, Z. Ge, S. S. Jain, M. S. Dodd, and L. Brandt, “Droplets in homogeneous shear turbulence,” J. Fluid Mech., vol. 876, pp. 962–984, 2019.
[14] T. Trummler, A. Begemann, E. Trautner, and M. Klein, “Numerical investigation of the segregation of turbulent emulsions,” Phys. Fluids (1994), vol. 34, no. 11, p. 113324, 2022.
[15] W. Aniszewski et al., “PArallel, robust, interface simulator (PARIS),” Comput. Phys. Commun., vol. 263, no. 107849, p. 107849, 2021.
[16] M. Crialesi-Esposito, L. A. Gonzalez-Montero, and F. J. Salvador, “Effects of isotropic and anisotropic turbulent structures over spray atomization in the near field,” Int. J. Multiph. Flow, vol. 150, no. 103891, p. 103891, 2022.
[17] Y. Ling, D. Fuster, G. Tryggvason, and S. Zaleski, “A two-phase mixing layer between parallel gas and liquid streams: multiphase turbulence statistics and influence of interfacial instability,” J. Fluid Mech., vol. 859, pp. 268–307, 2019.
[18] D. Jiang and Y. Ling, “Impact of inlet gas turbulence on the formation, development and breakup of interfacial waves in a two-phase mixing layer,” J. Fluid Mech., vol. 921, no. A15, 2021.